DISK POSITION NONLINEARITY EFFECTS ON THE CHAOTIC BEHAVIOR OF ROTATING FLEXIBLE SHAFT-DISK SYSTEMS

H. M. Khanlo *

Department of Aerospace Engineering
Aeronautical University of Science and Technology
Tehran 13846-73411, Iran

M. Ghayour S. Ziaei-Rad

Department of Mechanical Engineering
Isfahan University of Technology
Isfahan 84156-83111, Iran

ABSTRACT

This study investigates the effects of disk position nonlinearities on the nonlinear dynamic behavior of a rotating flexible shaft-disk system. Displacement of the disk on the shaft causes certain nonlinear terms which appears in the equations of motion, which can in turn affect the dynamic behavior of the system. The system is modeled as a continuous shaft with a rigid disk in different locations. Also, the disk gyroscopic moment is considered. The partial differential equations of motion are extracted under the Rayleigh beam theory. The assumed modes method is used to discretize partial differential equations and the resulting equations are solved via numerical methods. The analytical methods used in this work are inclusive of time series, phase plane portrait, power spectrum, Poincaré map, bifurcation diagrams, and Lyapunov exponents. The effect of disk nonlinearities is studied for some disk positions. The results confirm that when the disk is located at mid-span of the shaft, only the regular motion (period one) is observed. However, periodic, sub-harmonic, quasi-periodic, and chaotic states can be observed for situations in which the disk is located at places other than the middle of the shaft. The results show nonlinear effects are negligible in some cases.

Keywords: Rotating shaft, Dynamic behavior, Nonlinearities, Bifurcation, Chaotic, Gyroscopic.

1. INTRODUCTION

Many physical phenomena in the real world can be regarded as nonlinear, however, most of them can be simplified as a linear form with an accurate linearization technique. Such simplifications are usually unsuitable for high power and high-speed rotational systems whose application during the design and analysis may result in a mistake or potentially undesirable operation. The rotating shaft-disk system includes nonlinear subsystems such as nonlinear elastic elements, nonlinear damping, fluid related forces and nonlinear boundary conditions, which might affect the dynamic behavior of the system. This can take the form of high amplitude responses leading to fatigue or catastrophic failure; hence, the importance of identifying such undesirable behavior.

In recent years, many studies have been devoted to examining the nonlinear dynamic behavior of rotating systems due to different types of nonlinearities. A comprehensive review, especially of nonlinearities in bearings widely used in rotating machinery, can be found in [1]. Chang *et al.* [2] studied the nonlinear dynamic behavior and stability of rotating shaft-disk systems. They showed that prediction of the instability region is different for the linear and nonlinear equations of motion. Hosseini *et al*. [3,4] investigated the nonlinear vibration behavior of rotating shafts with stretching nonlinearity and nonlinearity in curvature and inertia. Łuczko [5] proposed a method for modeling geometrically nonlinear rotating shafts. His method is useful for detecting the bifurcation points and applicable to some more complex cases that are difficult to analyze by analytical methods. Qian *et al.* [6] studied the bifurcation of a rotating shaft with nonlinearity of the internal friction force. Their study shows that the stability of the rotating shaft can be improved by increasing external damping. Pavlović *et al.* [7] studied the effect of some parameters such as rotary inertia, damping coefficient and external-internal damping ratio on the stability of the rotating shaft using the direct Lyaponov method. Dimentberg *et al.* [8] studied the nonlinear vibration of Jeffcott rotor with stiffening nonlinearity. Cheng *et al.* [9] studied the rotor-bearing-seal system. They used a simple Jeffcott model for analyzing the effect of nonlinearities due to oil film and seal forces on the dynamic behavior of the system. Also, the bearing characteristics can be introduced as the nonlinearities that affect the behavior of rotors. Some works [10-12] presented the rotors behavior with bearing nonlinearities. The obtained results show the possibility of changing the regular rotor motion to irregular one subject to bearing forces. In these studies, the rotor model is discrete and the rotor

* Corresponding author (khanloh47@yahoo.com)

DOI : 10.1017/jmech.2012.61
Copyright © 2012 The Society of Theoretical and Applied Mechanics, R.O.C.
https://doi.org/10.1017/jmech.2012.61 Published online by Cambridge University Press

mass and bearing mass are assumed to lump at the mid-span of the shaft and the bearing, respectively. Also, when mounted at a distance from the shaft mid-span, the disk will not be co-linear with the shaft and their elementary centrifugal forces will, therefore, form an equivalent couple during rotation. This phenomenon is generally referred to as a gyroscopic effect [13]. The gyroscopic moment and the nonlinearities that arise due to disk position on the shaft can lead to a chaotic motion.

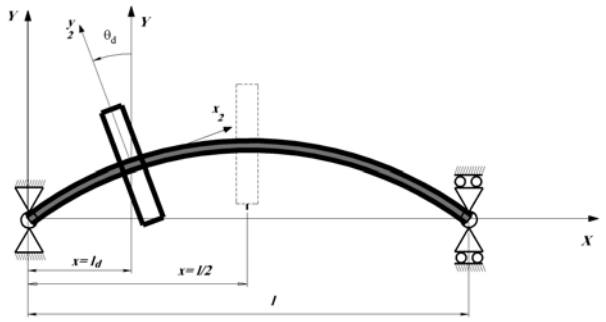
To the best of the authors' knowledge, no work has been reported so far on the chaotic behavior of rotating systems with consideration of the gyroscopic moment and also nonlinearities due to the disk position on the rotating shaft. In this paper, a continuous flexible shaft with a rigid disk in four positions is considered. The assumed modes method is used to discretize the partial differential equations of motion. The accuracy of the solution can be enhanced by including a higher number of modes. A rotating shaft-disk system is formulated including the Coriolis and centrifugal forces due to shaft flexibility. In addition, the nonlinearities and gyroscopic moment of the disk due to disk location is considered. Then, the nonlinear-coupled equations of motion are solved using numerical methods. Time series, phase plane portrait, power spectra, Poincaré map, bifurcation diagrams, and Lyapunov exponent are employed to investigate the behavior of the system. Finally, the numerical results obtained for the four scenarios are compared.

2. MATHEMATICAL FORMULATION

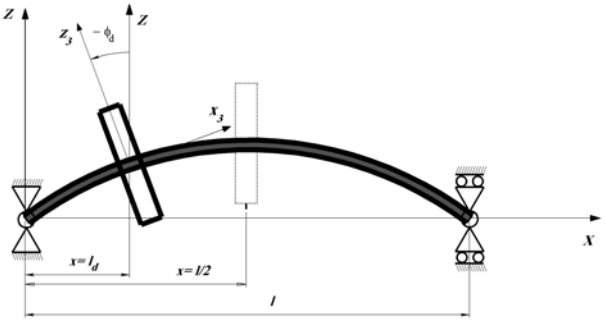
To investigate the shaft-disk system behavior, the following assumptions are made:

1. The uniform Rayleigh beam theory is used for mathematical modeling of the rotating shaft;
2. The shear deformation is neglected;
3. The shaft cross-section and material properties along its length are uniform, *i.e.* $I_y = I_z = I$;
4. The area moment inertia of the disk in the two principal directions is the same, *i.e.* $I_{yd} = I_{zd} = I_d$;
5. The internal damping is negligible;
6. The axial vibration and torsional is neglected.

Figure 1 shows the schematic of the rotating flexible shaft-disk system. The formulation of the problem is similar to that in our previous work [14]. However, in [14] disk nonlinear terms in the equations of motion neglected because of the disk was assumed to be located at the middle of the shaft. The chaotic behavior occurred due to the rub-impact. In this work, we deal with disk nonlinear terms and the rub-impact is not considered. The shaft rotates about the X axis at a angular velocity, Ω, relative to the inertial axes XYZ. The xyz coordinate is the body axes with x coinciding with the rotation axis, which is the spatial variable. The axes y and z rotate about axis $X = x$ together with the body at the same angular velocity $\omega = \Omega\mathbf{i}$. Also, the axes x_2, y_2 are obtained by rotation $\theta = v'(x, t)$ about



(a) *Y-X*



(b) *Z-X* plane view

Fig. 1 Rotating shaft-disk system; plane view

z axis and x_3, z_3 are obtained by rotation $\varphi = -w'(x, t)$ about y_2 axis, respectively. The bending positions of the shaft at any point of its neutral axis can be expressed by $v(x, t)$ and $w(x, t)$ along y and z, respectively. The angular velocity vector and neutral axis position vector of the shaft can be written in vector form as follows [15]:

$$\mathbf{r}_s = v(x,t)\,\mathbf{j} + w(x,t)\,\mathbf{k} \tag{1}$$

$$\mathbf{v}_s = \dot{\mathbf{r}}_s + \boldsymbol{\omega} \times \mathbf{r}_s \tag{2}$$

The velocity vector of a centerline of the shaft is

$$\mathbf{v}_s = \left(\dot{v}(x,t) - \Omega\, w(x,t)\right)\mathbf{j} + \left(\dot{w}(x,t) + \Omega\, v(x,t)\right)\mathbf{k} \tag{3}$$

The angular velocity vector of the shaft element is [16]:

$$\boldsymbol{\omega}_s = \left(\Omega - \dot{\theta}(x,t)\,\varphi(x,t)\right)\mathbf{i} + \left(-\Omega\,\theta(x,t) + \dot{\varphi}(x,t)\right)\mathbf{j} + \left(\Omega\varphi(x,t) + \dot{\theta}(x,t)\right)\mathbf{k} \tag{4}$$

where, $\theta(x, t)$ and $\phi(x, t)$ are the slopes of the flexible shaft and defined as

$$\theta = \frac{\partial v(x,t)}{\partial x} = v'(x,t)\ ,\ \varphi = -\frac{\partial w(x,t)}{\partial x} = -w'(x,t) \tag{5}$$

and l is the shaft length. $\dot{(\,)}$ and $()'$ denote differentiation with respect to time and displacement x, respectively.

Suppose that the disk is mounted on the shaft at an arbitrary point, $x = l_d$; hence, the position vector and velocity vector of the disk center are

https://doi.org/10.1017/jmech.2012.61 Published online by Cambridge University Press

$$\mathbf{r}_d = \big(v(x,t)\big)\mathbf{j} + \big(w(x,t)\big)\mathbf{k} \,\big|_{x=l_d} \tag{6}$$

$$\mathbf{v}_d = \big(\dot{v}(x,t) - \Omega w(x,t)\big)\mathbf{j} + \big(\dot{w}(x,t) + \Omega v(x,t)\big)\mathbf{k} \,\big|_{x=l_d} \tag{7}$$

The angular velocity vector of the disk is

$$\begin{aligned}\boldsymbol{\omega}_d = &\big(\Omega - \dot{\theta}(x,t)\varphi(x,t)\big)\mathbf{i} + \big(-\Omega\theta(x,t) + \dot{\varphi}(x,t)\big)\mathbf{j} \\ &+ \big(\Omega\varphi(x,t) + \dot{\theta}(x,t)\big)\mathbf{k} \,\big|_{x=l_d}\end{aligned} \tag{8}$$

The kinetic energy expression of a rotating shaft is

$$\begin{aligned}KE_s &= \frac{1}{2}\int_0^L (\rho A \dot{\mathbf{r}}_s^T \dot{\mathbf{r}}_s + \rho \boldsymbol{\omega}_s^T \mathbf{I} \boldsymbol{\omega}_s)\, dx \\ &= \frac{1}{2}\int_0^L \Big[\rho A\Big(\big(\dot{v}(x,t) - \Omega w(x,t)\big)^2 + \big(\dot{w}(x,t) + \Omega v(x,t)\big)^2\Big) \\ &\quad + \rho\Big(I_y\big(\Omega v'(x,t) + \dot{w}'(x,t)\big)^2 + I_z\big(-\Omega w'(x,t) + \dot{v}'(x,t)\big)^2 \\ &\quad + J_p\big(\Omega + v'(x,t)\dot{w}'(x,t)\big)^2\Big)\Big]\, dx\end{aligned} \tag{9}$$

where, ρ is shaft mass density, A is the cross-section area and I_y, I_z and J_p are the diametral area moment of inertia in the y and z directions and the polar area moment of inertia and of the shaft, respectively.

The kinetic energy expression of a rigid disk is

$$\begin{aligned}KE_d = \frac{1}{2}\Big[&m_d\Big(\big(\dot{v}(x,t) - \Omega w(x,t)\big)^2 + \big(\dot{w}(x,t) + \Omega v(x,t)\big)^2\Big) \\ &+ \rho_d\, h\big(I_{yd}\big(\Omega v'(x,t) + \dot{w}'(x,t)\big)^2 \\ &+ I_{zd}\big(-\Omega w'(x,t) + \dot{v}'(x,t)\big)^2 \\ &+ J_{pd}\big(\Omega + v'(x,t)\,\dot{w}'(x,t)\big)^2\big)\Big]\Big|_{x=x_d}\end{aligned} \tag{10}$$

where, ρ_d is disk mass density and m_d, h, I_{yd}, I_{zd} and J_{pd} are mass, disk thickness, diametral area moment of inertia in y and z direction and polar area moment of inertia of the disk, respectively. Since the shaft has a circular cross-section, its polar area moment of inertia is twice its diametrical area moment of inertia. The same also applies to the disk. The total kinetic energy of the system is the sum of T_s and T_d.

The strain energy due to the bending alone is

$$PE = \frac{1}{2}\int_0^l \big(E I_y \big(w''(x,t)\big)^2 + E I_z \big(v''(x,t)\big)^2\big)\, dx \tag{11}$$

In addition, the dissipation energy of the system is

$$F = \frac{1}{2}\int_0^l C\Big(\big(\dot{v}(x,t)\big)^2 + \big(\dot{w}(x,t)\big)^2\Big)\, dx \tag{12}$$

where, C is the external damping coefficient per unit length. To derive the equations of motion, it is convenient to use the assumed mode method and to define displacements as follows

$$v(x,t) = \sum_{i=1}^{n} \Psi_i(x)\, \mathrm{V}_i(t) = \boldsymbol{\Psi}^{\mathrm{T}}(x)\,\mathbf{V}(t) \tag{13}$$

$$w(x,t) = \sum_{i=1}^{n} \Psi_i(x)\ \ \mathrm{W}_i(t) = \boldsymbol{\Psi}^{\mathrm{T}}(x)\,\mathbf{W}(t) \tag{14}$$

where, $\boldsymbol{\Psi}(x)$ is the admissible spatial function vector which describes the transverse deflections of the shaft, and $\mathbf{V}(t)$ and $\mathbf{W}(t)$ are the column vectors consisting of the corresponding time-dependent generalized coordinates.

The Lagrangian may be expressed as

$$L = KE_s + KE_d - PE \tag{15}$$

Substituting Eqs. (13) and (14) into Eqs. (9 ~ 12), the discrete form of the Lagrangian is obtained as Eq. (A1). The Lagrange equation is expressed as

$$\frac{d}{dt}\left(\frac{\partial L}{\partial \dot{q}_i}\right) - \left(\frac{\partial L}{\partial q_i}\right) + \left(\frac{\partial F}{\partial \dot{q}_i}\right) = Q_i\ ,\ \ i = 1,\ 2,\ 3,\ \ldots \tag{16}$$

Application of the Lagrange equation, and after some manipulations [15], the simplified equations of motion can be rewritten as

$$\mathbf{M}\ddot{\mathbf{q}} + \mathbf{h}(\mathbf{q}, \dot{\mathbf{q}}) = \mathbf{Q} \tag{17}$$

where, $\mathbf{M}$ is mass matrix, $\mathbf{q} = [\mathbf{V}\ \mathbf{W}]^{\mathbf{T}}$ designates the generalized coordinates, and $\mathbf{Q} = [\mathbf{Q_v}\ \mathbf{Q_W}]$ designates the generalized forces, that comprises the disk unbalance and gravitational forces.

Let us define the non-dimensional parameters as

$$\mathbf{v} = \frac{\mathbf{V}}{h},\ \ \mathbf{w} = \frac{\mathbf{W}}{h},\ \ \tau = \Omega t\ ,\ \ \frac{d}{dt} = \Omega\frac{d}{d\tau},$$
$$S = \frac{\Omega}{\omega_n},\ \ C_T = \frac{C}{2\kappa^2\sqrt{\rho A(EI/l^4)}},\ \ \gamma = \frac{C_T}{S},$$

And constant coefficients as

$$\alpha_{1s} = \frac{I_y}{A},\ \ \alpha_{2s} = \frac{I_z}{A},\ \ \alpha_{3s} = \frac{J_p}{A},\ \ \beta = \frac{2l^4}{\kappa^4},$$
$$\omega_n^2 = \kappa^4\frac{EI}{\rho A l^4},\ \ \alpha_{1d} = \frac{\rho_d\, h\, I_{yd}}{\rho A},\ \ \alpha_{2d} = \frac{\rho_d\, h\, I_{zd}}{\rho A},$$
$$\alpha_{3d} = \frac{\rho_d\, h\, J_{pd}}{\rho A},\ \ \zeta = \frac{m_d}{\rho A},\ \ \eta_s = \frac{J_p\, h^2}{A},$$
$$\eta_d = \frac{\rho_d\, J_{pd}\, h^2}{\rho A},\ \ p = \rho A h \Omega^2$$

where κ is constant that depends on the boundary conditions.

Now, one can rewrite the simplified non-dimensional form of Eq. (17) as

$$\tilde{\mathbf{M}}\ddot{\tilde{\mathbf{q}}} + \tilde{\mathbf{h}}(\tilde{\mathbf{q}}, \dot{\tilde{\mathbf{q}}}) = \tilde{\mathbf{Q}} \tag{18}$$

$$\tilde{\mathbf{M}} = \begin{bmatrix} \tilde{\mathbf{M}}_{11} & \tilde{\mathbf{M}}_{12} \\ \tilde{\mathbf{M}}_{21} & \tilde{\mathbf{M}}_{22} \end{bmatrix} \tag{19}$$

https://doi.org/10.1017/jmech.2012.61 Published online by Cambridge University Press

$$\tilde{\mathbf{M}}_{11} = \mathbf{I} + \alpha_{2s}\,\mathbf{\Lambda}_1^{-1}\mathbf{\Lambda}_2 + \zeta\mathbf{\Lambda}_1^{-1}\mathbf{\Lambda}_{d1} + \alpha_{2d}\,\mathbf{\Lambda}_1^{-1}\mathbf{\Lambda}_{d2} \tag{20}$$

$$\tilde{\mathbf{M}}_{12} = \tilde{\mathbf{M}}_{21} = \mathbf{0} \tag{21}$$

$$\begin{aligned}\tilde{\mathbf{M}}_{22} &= \mathbf{I} + \alpha_{1s}\,\mathbf{\Lambda}_1^{-1}\mathbf{\Lambda}_2 + \underline{\eta_s\,\mathbf{\Lambda}_1^{-1}\left(\mathbf{Int}(\mathbf{\Psi}'\mathbf{\Psi}'^{T}\mathbf{v}\,\mathbf{v}^{\mathrm{T}}\mathbf{\Psi}'\mathbf{\Psi}'^{\mathrm{T}})\right)} \\ &+\zeta\mathbf{\Lambda}_1^{-1}\mathbf{\Lambda}_{d1} + \alpha_{1d}\,\mathbf{\Lambda}_1^{-1}\mathbf{\Lambda}_{d2} + \underline{\underline{\eta_d\,\mathbf{\Lambda}_1^{-1}\left(\mathbf{Int}(\mathbf{\Psi}'_d\,\mathbf{\Psi}'^{\mathrm{T}}_d\mathbf{v}\,\mathbf{v}^{\mathrm{T}}\mathbf{\Psi}'_d\,\mathbf{\Psi}'^{\mathrm{T}}_d)\right)}}\end{aligned} \tag{22}$$

$$\tilde{\mathbf{H}} = \tilde{\mathbf{Q}} - \tilde{\mathbf{h}} = \left[\tilde{\mathbf{h}}_v(\tilde{\mathbf{q}},\dot{\tilde{\mathbf{q}}}) \quad \tilde{\mathbf{h}}_w(\tilde{\mathbf{q}},\dot{\tilde{\mathbf{q}}})\right]^{\mathrm{T}} \tag{23}$$

$$\begin{aligned}\tilde{\mathbf{h}}_v = &\frac{\mathbf{\Lambda}_1^{-1}}{p}\mathbf{Q}_v - (-2\dot{\mathbf{w}} - \mathbf{v} + \alpha_{2s}\,\mathbf{\Lambda}_1^{-1}\mathbf{\Lambda}_2\dot{\mathbf{w}} - \alpha_{3s}\,\mathbf{\Lambda}_1^{-1}\mathbf{\Lambda}_2\dot{\mathbf{w}} \\ &- \alpha_{1s}\,\mathbf{\Lambda}_1^{-1}\mathbf{\Lambda}_2\mathbf{v} + \alpha_{1s}\,\mathbf{\Lambda}_1^{-1}\mathbf{\Lambda}_2\dot{\mathbf{w}} \\ &+ \frac{\beta}{S^2}\mathbf{\Lambda}_1^{-1}\mathbf{\Lambda}_3\mathbf{v} + \frac{C_T}{S}\dot{\mathbf{v}} \\ &- \underline{\eta_s\,\mathbf{\Lambda}_1^{-1}\left(\mathbf{Int}(\mathbf{\Psi}'\mathbf{\Psi}'^{\mathrm{T}}\mathbf{v}\,\dot{\mathbf{w}}^{\mathrm{T}}\mathbf{\Psi}'\mathbf{\Psi}'^{\mathrm{T}}\dot{\mathbf{w}})\right)} \\ &- 2\zeta\mathbf{\Lambda}_1^{-1}\mathbf{\Lambda}_{d1}\,\dot{\mathbf{w}} + \alpha_{2d}\,\mathbf{\Lambda}_1^{-1}\mathbf{\Lambda}_{d2}\,\dot{\mathbf{w}} \\ &- \zeta\mathbf{\Lambda}_1^{-1}\mathbf{\Lambda}_{d1}\,\mathbf{v} - \alpha_{3d}\,\mathbf{\Lambda}_1^{-1}\mathbf{\Lambda}_{d2}\,\dot{\mathbf{w}} - \alpha_{1d}\,\mathbf{\Lambda}_1^{-1}\mathbf{\Lambda}_{d2}\,\mathbf{v} \\ &+ \alpha_{1d}\,\mathbf{\Lambda}_1^{-1}\mathbf{\Lambda}_{d2}\,\dot{\mathbf{w}} - \underline{\underline{\eta_d\,\mathbf{\Lambda}_1^{-1}\left(\mathbf{Int}(\mathbf{\Psi}'_d\mathbf{\Psi}'^{\mathrm{T}}_d\mathbf{v}\,\dot{\mathbf{w}}^{\mathrm{T}}\mathbf{\Psi}'_d\mathbf{\Psi}'^{\mathrm{T}}_d\,\mathbf{w})\right)}}\end{aligned} \tag{24}$$

$$\begin{aligned}\tilde{\mathbf{h}}_w = &\frac{\mathbf{\Lambda}_1^{-1}}{p}\mathbf{Q}_w - (2\dot{\mathbf{v}} - \mathbf{w} - \alpha_{1s}\,\mathbf{\Lambda}_1^{-1}\mathbf{\Lambda}_2\dot{\mathbf{v}} + \alpha_{3s}\,\mathbf{\Lambda}_1^{-1}\mathbf{\Lambda}_2\dot{\mathbf{v}} \\ &- \alpha_{2s}\,\mathbf{\Lambda}_1^{-1}\mathbf{\Lambda}_2\mathbf{w} - \alpha_{2s}\,\mathbf{\Lambda}_1^{-1}\mathbf{\Lambda}_2\dot{\mathbf{v}} \\ &+ \frac{\beta}{S^2}\mathbf{\Lambda}_1^{-1}\mathbf{\Lambda}_3\,\mathbf{w} + \frac{C_T}{S}\dot{\mathbf{w}} + \underline{\eta_s\,\mathbf{\Lambda}_1^{-1}\left(\mathbf{Int}(\mathbf{\Psi}'\,\mathbf{\Psi}'^{\mathrm{T}}\dot{\mathbf{v}}\,\mathbf{v}^{\mathrm{T}}\mathbf{\Psi}'\,\mathbf{\Psi}'^{\mathrm{T}}\dot{\mathbf{w}})\right)} \\ &+ \underline{\eta_s\,\mathbf{\Lambda}_1^{-1}\left(\mathbf{Int}(\mathbf{\Psi}'\mathbf{\Psi}'^{\mathrm{T}}\mathbf{v}\,\dot{\mathbf{v}}^{\mathrm{T}}\mathbf{\Psi}'\mathbf{\Psi}'^{\mathrm{T}}\dot{\mathbf{w}})\right)} \\ &+ 2\zeta\mathbf{\Lambda}_1^{-1}\mathbf{\Lambda}_{d1}\,\dot{\mathbf{v}} - \alpha_{1d}\,\mathbf{\Lambda}_1^{-1}\mathbf{\Lambda}_{d2}\,\dot{\mathbf{v}} - \zeta\mathbf{\Lambda}_1^{-1}\mathbf{\Lambda}_{d1}\,\mathbf{w} + \alpha_{3d}\,\mathbf{\Lambda}_1^{-1}\mathbf{\Lambda}_{d2}\,\dot{\mathbf{v}} \\ &- \alpha_{2d}\,\mathbf{\Lambda}_1^{-1}\mathbf{\Lambda}_{d2}\,\mathbf{w} - \alpha_{2d}\,\mathbf{\Lambda}_1^{-1}\mathbf{\Lambda}_{d2}\,\dot{\mathbf{v}} \\ &+ \underline{\eta_d\,\mathbf{\Lambda}_1^{-1}\left(\mathbf{Int}(\mathbf{\Psi}'_d\,\mathbf{\Psi}'^{\mathrm{T}}_d\dot{\mathbf{v}}\,\mathbf{v}^{\mathrm{T}}\mathbf{\Psi}'_d\,\mathbf{\Psi}'^{\mathrm{T}}_d\dot{\mathbf{w}})\right)} \\ &+ \underline{\underline{\eta_d\,\mathbf{\Lambda}_1^{-1}\left(\mathbf{Int}(\mathbf{\Psi}'_d\,\mathbf{\Psi}'^{\mathrm{T}}_d\mathbf{v}\,\dot{\mathbf{v}}^{\mathrm{T}}\mathbf{\Psi}'_d\,\mathbf{\Psi}'^{\mathrm{T}}_d\dot{\mathbf{w}})\right)}}\end{aligned} \tag{25}$$

where Λ_1, Λ_2, Λ_3, Λ_{d1}, Λ_{d2} are constant matrices presented in Appendix A (Eqs. A.2 ~ A.6). The once-underlined and twice-underlined nonlinear terms in the above Eqs. are related to the shaft and disk, respectively. Also, the sign (**Int.**) in Eqs. (22 ~ 25) denote the integration with respect to x. Equation (18) describes the coupled nonlinear differential equation governing the flexible shaft-disk motion.

3. NUMERICAL RESULTS AND DISCUSSION

The numerical analysis of Eq. (18) is carried out a variable step continuous solver based on the Runge-Kutta (5,4) formula. The main point in obtaining reliable results is to select proper time steps for the numerical integration as well as proper number of modes for the continuous system [17]. In this work a variable time step and three modes is used for numerical analyses. The numerical results showed that the use of three modes guarantee the convergence of numerical results. The non-dimensional speed ratio, S, is used as a control parameter. The mode shapes of the non-rotating uniform beam with simply supported boundary conditions at both ends are used as the admissible functions for the flexible shaft-disk system [18].

$$\psi_i(x) = \sqrt{2}\sin\left(\frac{i\pi x}{l}\right), \quad i = 1, 2, 3, \cdots \tag{26}$$

To guarantee that the data being used are in a steady state, the first few hundred-time series data of the integration have been neglected. The results of the next few hundred time series are retained to carry out the analysis. The numerical simulation is carried out in the following four scenarios:

Scenario 1: The disk is located at $x = l_d = l/4$.

Scenario 2: The disk is located at $x = l_d = l/3$.

Scenario 3: The disk is located at $x = l_d = 2l/5$.

Scenario 4: The disk is located at $x = l_d = l/2$.

The values for the constant and non-dimensional parameters of the system used in the analysis are

$\alpha_{1s} = \alpha_{2s} = 56\,(\mathrm{mm}^2)$, $\alpha_{3s} = 1.12\times10^2\,(\mathrm{mm}^2)$,
$\beta = 2.1\times10^{10}\,(\mathrm{mm}^4)$, $C_T = 0.372$,
$\alpha_{3d} = 3.87\times10^6\,(\mathrm{mm}^3)$, $\alpha_{1d} = \alpha_{2d} = 1.94\times10^5\,(\mathrm{mm}^3)$,
$\zeta = 1.94\times10^3\,(\mathrm{mm})$, $\eta_s = 1.12\times10^3\,(\mathrm{mm}^4)$,
$\eta_d = 3.9\times10^7\,(\mathrm{mm}^4)$

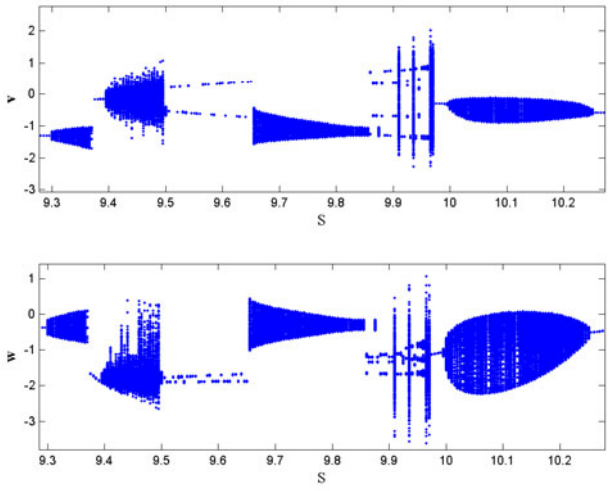
Then, the effect of nonlinearities introduced due to disk location on the chaotic motion of the system is studied.

3.1 Bifurcation Diagram

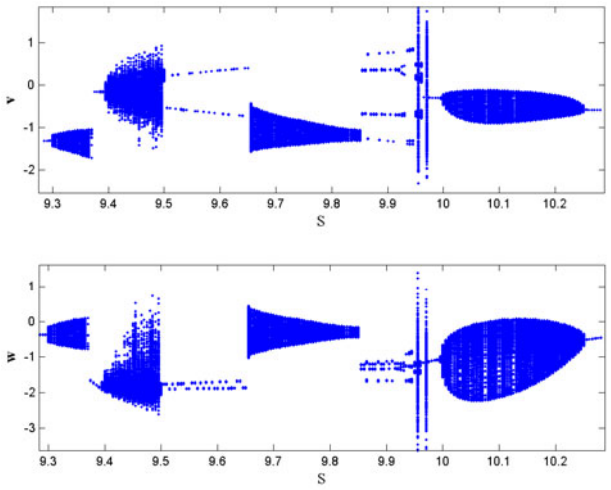
To generate the bifurcation diagram, the system control parameter (*i.e.*; speed ratio (S)) is varied with a fixed step and the state variables at the end of each step are used as initial conditions for the next step. These data points are then plotted versus the rotational speed ratio. If the motion is regular (synchronous) at the specific rotational speed ratio, the bifurcation diagram then contains finite single points. When the motion is quasi-periodic or chaotic, the data points in the bifurcation diagram are distributed along a line.

The bifurcation diagram of the system in scenario 1 is shown in Fig. 2(a). In this scenario, the dynamic behavior of the system is regular with period-one (1T) until $S = 9.29$. The regular motion suddenly bifurcates to the chaotic attractor at $S = 9.30$. This type of bifurcation can be classified as an explosive bifurcation [19,20]. This situation is maintained up to $S = 9.36$. The irregular motion of the system bifurcates to a sub- harmonic motion with the period 7T at $S = 9.37$. The behavior of the system at $S = 9.375$ jumps to another regular attractor with period-one. Since the system response jumps to the remote attractor, the bifurcation point can be classified as dangerous bifurcation. Again, the motion of the system becomes irregular (chaotic) at $S = [9.395 \sim 9.50]$. The system becomes super-harmonic at $S = [9.50 \sim 9.65]$. The behavior of the system varies between quasi-periodic and chaotic alternatively at $S = [9.65 \sim 9.86]$.

https://doi.org/10.1017/jmech.2012.61 Published online by Cambridge University Press

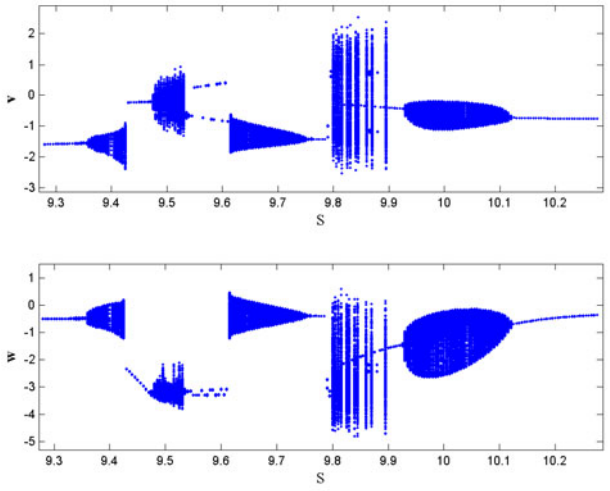


(a) With increasing S

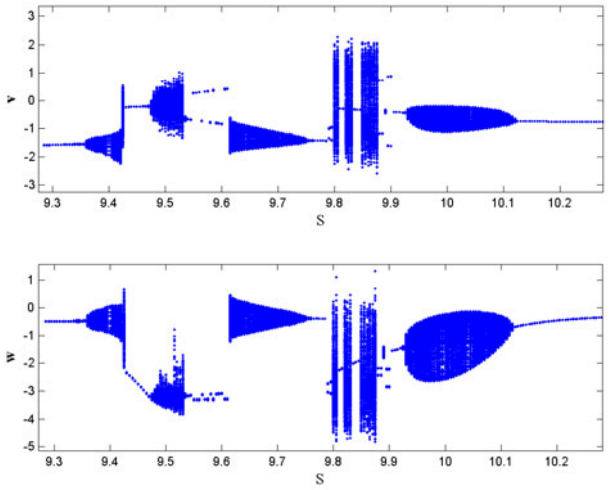


(b) With decreasing S

Fig. 2 The bifurcation diagram of the system for Scenario 1 ($x = l_d = l/4$)



(a) With increasing S



(b) With decreasing S

Fig. 3 The bifurcation diagram of the system for Scenario 2 ($x = l_d = l/3$)

It gets into the sub- harmonic motion with period-2 ($2T$) at $S = [9.86 \sim 9.92]$. The period doubling occurs at end of the preceding region, and period-2 ($2T$) becomes period-4 ($4T$). This region is maintained up to $S = 9.935$. The other chaotic motion occurs at $S = 9.935$. It gets back again into a period-4 ($4T$) at $S = [9.35 \sim 9.65]$. The chaotic motion occurs again at $S = [9.965 \sim 9.975]$. At $S = 9.975$, the chaotic region suddenly becomes regular (period-1). The regular motion explodes into the quasi-periodic attractor at $S = 9.995$, becoming regular (period-1) beyond $S = 10.25$.

A comparison of the bifurcation diagram in Figs. 2(a) ~ 2(b) for increasing and decreasing, S, shows the existence of multiple attractors for certain speed ratio ranges, *i.e.* $S = [9.86 \sim 9.97]$. The bifurcation diagrams Figs. 2(a) ~ 2(b), do not reveal all the possible responses of the rotor, unless one performs a large set of numerical simulations over a wide range of initial conditions.

In scenario 2, shown in Fig. 3(a), the regular motion (period-1) of the system suddenly bifurcates to a quasi-periodic motion at $S = 9.355$. This behavior exists up to $S = 9.425$, except at $S = 9.40$ in which the motion is regular with finite peaks. The response of the system at this irregular attractor jumps to the remote regular (period-1) attractor. At $S = 9.475$, the system suddenly exhibits an irregular (chaotic) motion and subsequently becomes regular (super-harmonic) at $S = [9.535 \sim 9.615]$. The second irregular region is observed at $S = [9.615 \sim 9.76]$. This irregular attractor gets into a regular motion ($1T$ and $2T$) again at $S = [9.76 \sim 9.80]$. At $S = [9.80 \sim 10.93]$, behavior of the system oscillates between regular motion ($1T$) and chaotic motion alternatively. At $S = [9.93 \sim 10.13]$ there is a quasi-periodic motion and finally the system becomes period-1 at $S = 10.13$.

Also, a comparison of the bifurcation diagram in Figs. 3(a) ~ 3(b) for increasing and decreasing, S, shows co-existence of different attractors for certain speed ratio ranges, $S = [9.785 \sim 9.905]$. Since the coefficient of the disk nonlinear terms (twice- underlined), changes due to disk positions (that are related to disk slop) on the shaft. However, the disk position changing on the shaft, can be affect the coefficients of related nonlinear terms and thereby the dynamic behavior of the system. As the results when the disk mounted at

https://doi.org/10.1017/jmech.2012.61 Published online by Cambridge University Press

position other than the shaft mid-span, it cannot be ignore the nonlinear terms (especially scenarios 1 and 2 in the article).

In scenario 3 (Fig. 4), the dynamic behavior of the system is regular with period-1 up to $S = 9.74$. This regular attractor undergoes a dangerous bifurcation [19] around the first resonance and jumps to another regular attractor at $S = 9.745$. The response of the system is retained in the new regular attractor up to $S = 9.80$ to become quasi-periodic later at $S = [9.805 \sim 9.88]$. At $S = 9.885$, the system returns back to a regular (period-1) motion. In scenario 3 the slops of the disk decreases, that result in decreasing nonlinear coefficients and chaotic behavior.

In scenario 4, the effects of nonlinear terms due to disk position in the equations of motion are not prevalent since the disk is located at the mid-span of the shaft. So, the motion style is perfectly regular (periodic-1) as shown in Fig. 5. Thus, no irregular (quasi-periodic or chaotic) motion can be created by changing the speed ratio. In scenario 4 the slops of the disk vanishes, that result in vanishing the nonlinear coefficients and chaotic behavior.

The scenarios 3 and 4 do not show the existence of multiple attractors for increasing or decreasing, S.

3.2 Time Series

A time series is a sequence of data points calculated typically at successive times and spaced at uniform time intervals. When the envelope of a time series is flat, the motion is periodic; otherwise, it is periodic, quasi-periodic, or chaotic. Figures 6.1(a) to 7(a) exhibit the time series response of the system in the different scenarios studied. As shown, the time series response has one amplitude in period one, a finite amplitude in the sub-harmonic motion, and one non-detectable amplitude in chaotic motion.

3.3 Power Spectrum

The Fast Fourier Transform is applied to the dynamic response of the system in order to construct the power spectrum components of the motion. Figures 6.1(b) to 7(b) show the power spectrum of the system for the different scenarios examined. As an example, Fig. 6.1(b) reveals the power spectrum of the regular (period-1) motion that consists of a single basic frequency. Figure 6.2(b) shows the spectrum of a quasi-periodic motion attractor. The dynamic response of the system demonstrates the sub-harmonic motion of period $7T$ at a speed ratio of $S = 9.37$. As is shown in Fig. 6.3(b) the power spectrum at this speed ratio has a clear peak at the frequencies 1/7.

3.4 Poincaré Map

In non-autonomous systems, a point on the Poincaré section is referred to as the return points of the time series at the constant interval T, where T is the driving period of the exciting force. The projection of the Poincaré section on the phase plane is referred to as the

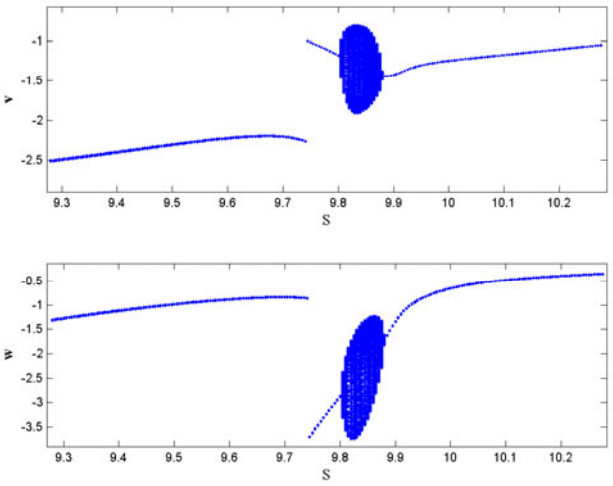


Fig. 4 The bifurcation diagram of the system for Scenario 3 ($x = l_d = 2l/5$)

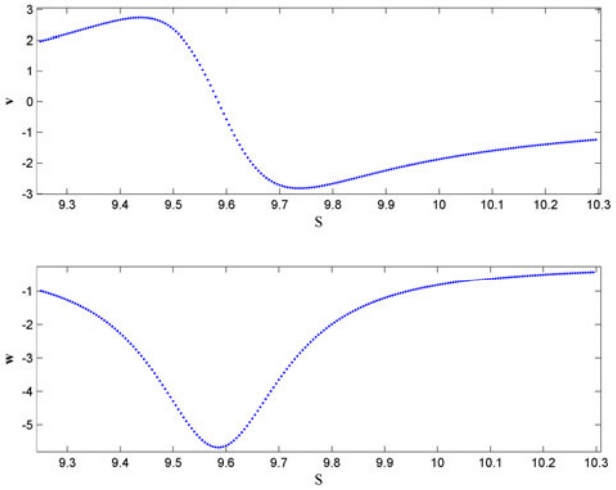


Fig. 5 The bifurcation diagram of the system for Scenario 4 ($x = l_d = l/2$)

Poincaré map. If we have k discrete return points, the corresponding motion will be periodic with the period k-T. For a quasi-periodic motion, the return points form a closed curve. For a chaotic motion, the return points on the Poincaré map form a geometrically fractal structure [19]. Figures 6.1(c) to 7(c) present the Poincaré map of the shaft-disk system. In Scenario 1, the regular motion of the system (period-1) is shown with a single point for $S = 9.29$ and the chaotic motion for $S = 9.48$, Fig. 6.4(c) has a fractal structure in Poincaré map. The four single points in the Poincaré map at $S = 9.93$ shown in Fig. 6.5(c) confirm the sub-harmonic (period-4) motion. The closed curve in the Poincaré map represents the quasi-periodic motion at $S = 9.34$, Fig. 6.2(c). Figures 7.1(c) and 7.2(c) reveal the existence of a regular motion with finite period and sub-harmonic motion (period-2) at $S = 9.40$ and $S = 9.79$, respectively. The chaotic attractor with the fractal structure in Scenario 2 is shown in Fig. 7.3(c).

https://doi.org/10.1017/jmech.2012.61 Published online by Cambridge University Press

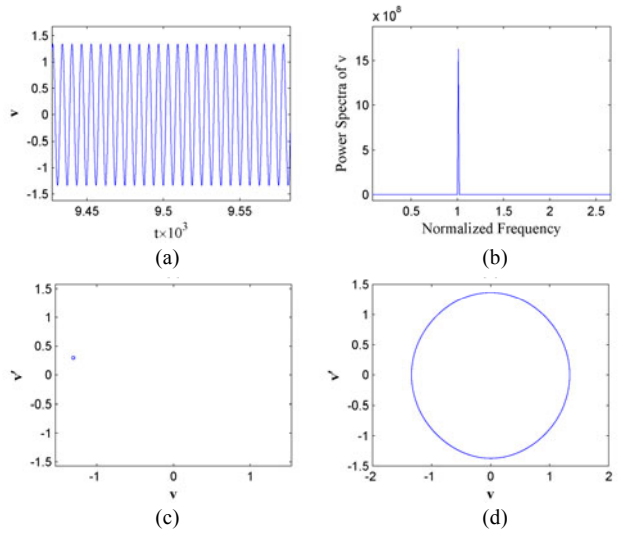


Fig. 6.1 (a) time series, (b) power spectrum, (c) Poincaré map, (d) phase plane portrait at $S = 9.29$, Scenario 1 ($x = l_d = l/4$)

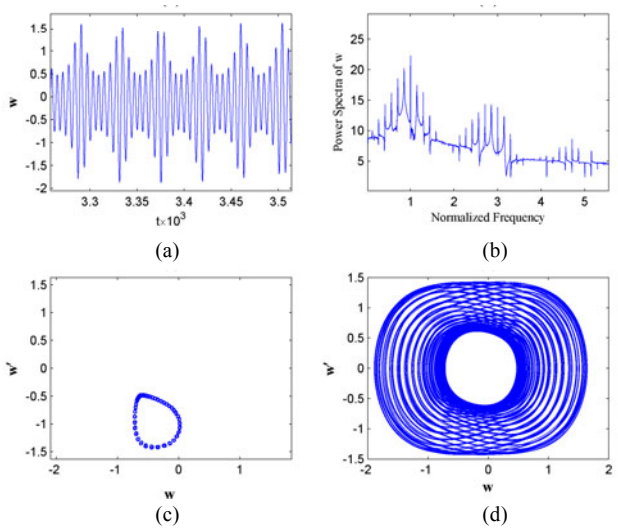


Fig. 6.2 (a) time series, (b) power spectrum, (c) Poincaré map, (d) phase plane portrait at $S = 9.34$, Scenario 1 ($x = l_d = l/4$)

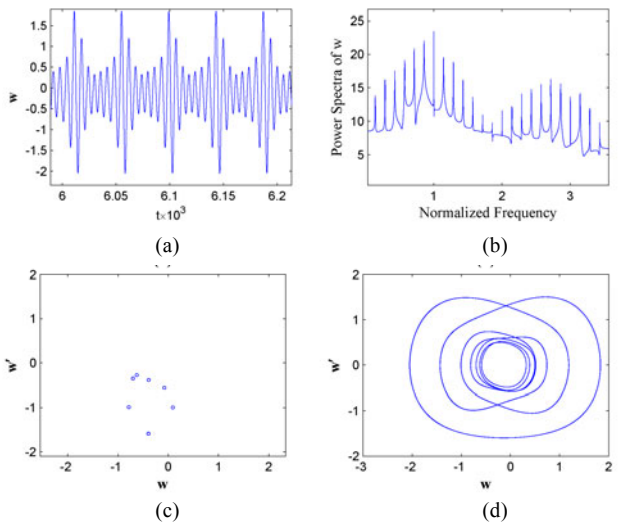


Fig. 6.3 (a) time series, (b) power spectrum, (c) Poincaré map, (d) phase plane portrait at $S = 9.37$, Scenario 1 ($x = l_d = l/4$)

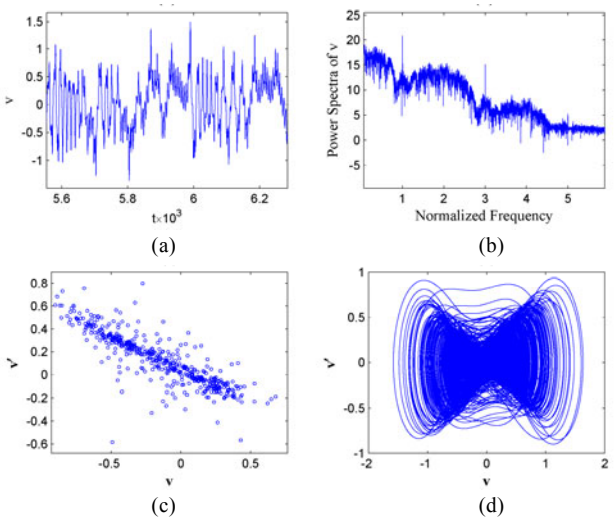


Fig. 6.4 (a) time series, (b) power spectrum, (c) Poincaré map, (d) phase plane portrait at $S = 9.48$, Scenario 1 ($x = l_d = l/4$)

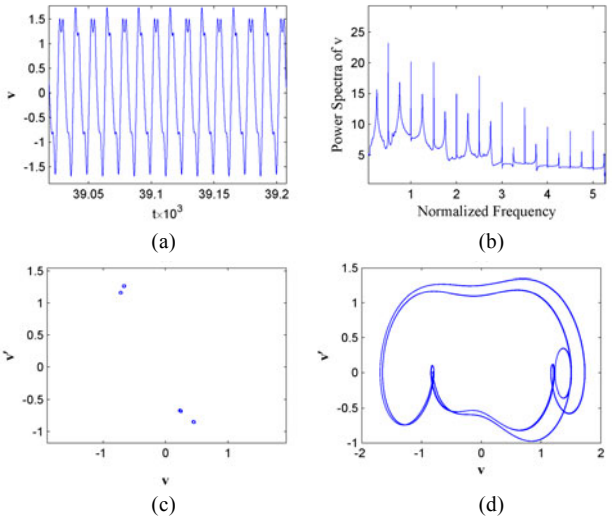


Fig. 6.5 (a) time series, (b) power spectrum, (c) Poincaré map, (d) phase plane portrait at $S = 9.93$, in Scenario 1 ($x = l_d = l/4$)

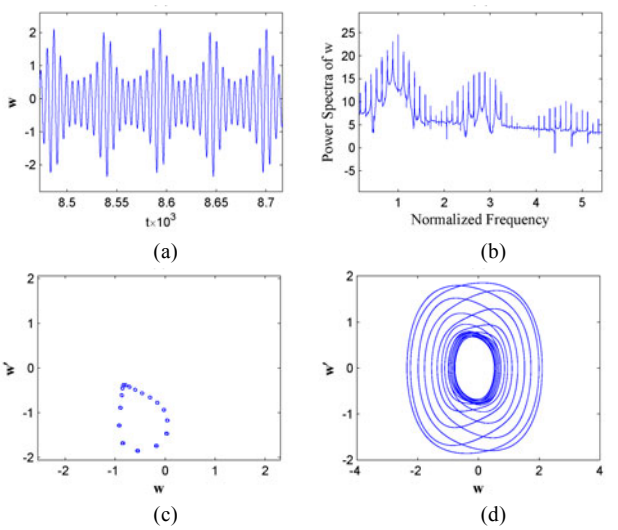


Fig. 7.1 (a) time series, (b) power spectrum, (c) Poincaré map, (d) phase plane portrait at $S = 9.40$, Scenario 2 ($x = l_d = l/3$)

https://doi.org/10.1017/jmech.2012.61 Published online by Cambridge University Press

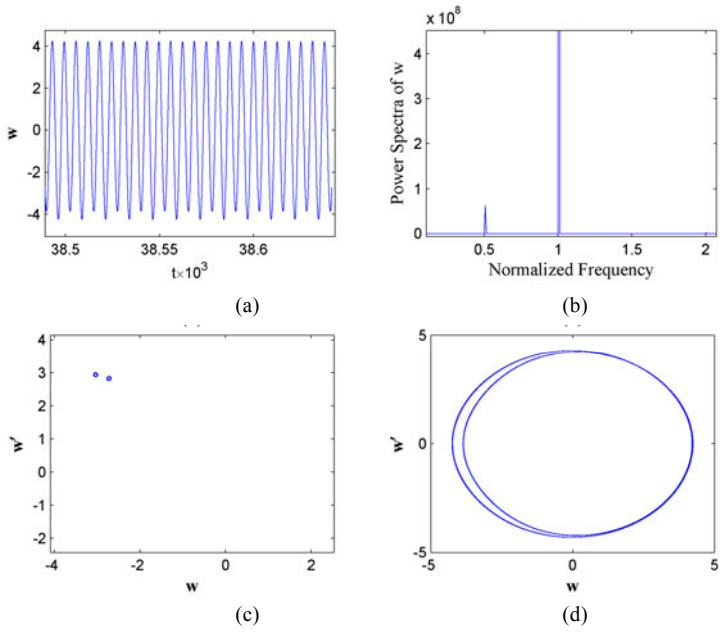


Fig. 7.2 (a) time series, (b) power spectrum, (c) Poincaré map, (d) phase plane portrait at $S = 9.79$, Scenario 2 ($x = l_d = l/3$)

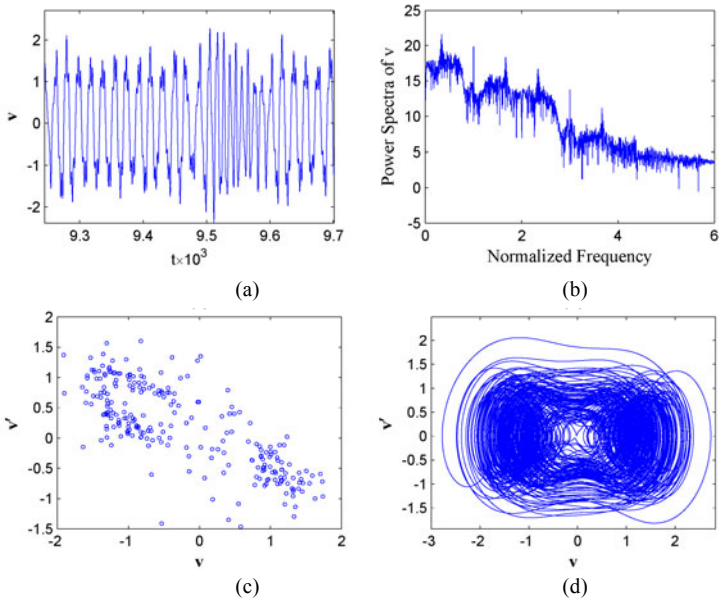


Fig. 7.3 (a) time series, (b) power spectrum, (c) Poincaré map, (d) phase plane portrait at $S = 9.80$, Scenario 2 ($x = l_d = l/3$)

3.5 Phase Plane Portrait

Figures 6.1(d) to 7.3(d) exhibit the phase plane portrait of the system in the different scenarios. As shown in these Figures, the regular motion (1T) is illustrated by one circle or ellipse. The presence of the sub-harmonic motion leads to distortions in the phase plane portrait. As an example, Fig. 6.5(d) shows the sub-harmonic motion with period four. As shown in Fig. 7.3(d), many crossings and loops are seen in the phase plane portrait, which is a signature of the chaotic motion.

3.6 Lyapunov Exponent

The Lyapunov exponents determine the average rate of the exponential expansion or contraction in the direction of an initial deviation $y(0)$ on a trajectory of the system, which is given by $\bar{\lambda}_i = \lim_{t\to\infty} \frac{1}{t} \ln\left(\| y(t) \| / \| y(0) \|\right)$, where the symbol $\| \ \|$ denotes a vector norm and $\bar{\lambda}_i$ is called the Lyapunov exponent. If the maximum Lyapunov exponent is negative or zero, there is a regular motion, and the positive maximum Lyapunov exponent confirms the chaotic motion [19,20]. The Lyapunov exponents of the Eq. (18) are obtained using the algorithm given in Ref. [21]. As displayed in Fig. 8, the maximum Lyapunov exponents at $S = 9.48$ and $S = 9.80$ in the respective Scenarios are positive, confirming the chaotic motion at given speed ratios. Thus, the maximum Lyapunov exponent is a useful tool for verifying the results of other nonlinear analytical tools used to identify chaotic behavior.

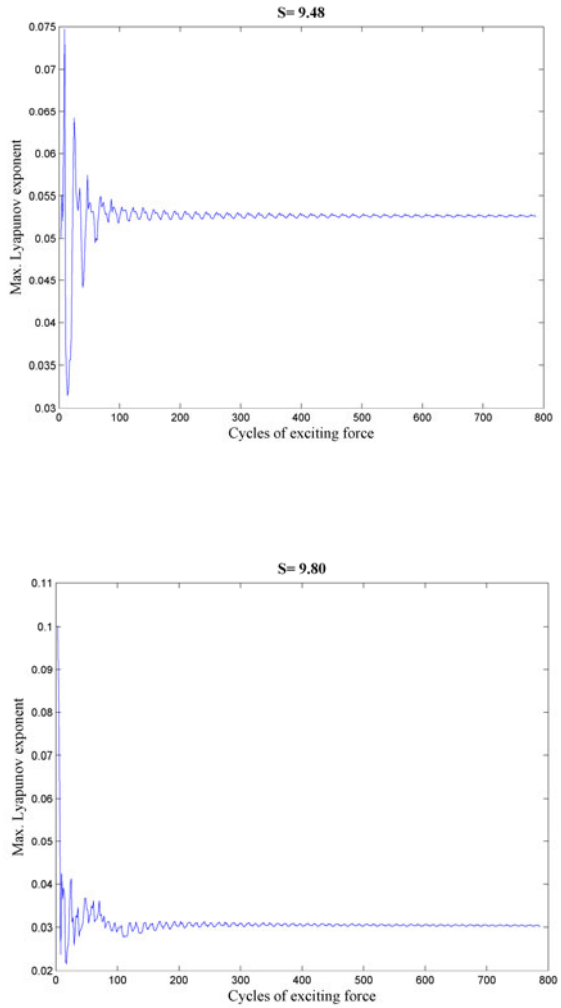


Fig. 8 The maximum Lyapunov exponents for Scenarios 1 and 2 in the given speed ratios

https://doi.org/10.1017/jmech.2012.61 Published online by Cambridge University Press

4. CONCLUSIONS

The nonlinear dynamic analysis of a system composed of a continuous flexible shaft with a rigid disk in four locations was presented in this work. The influence of the disk nonlinearities and the gyroscopic effects due to changing disk location on the shaft was studied. The assumed mode method was used to discretize the partial differential equations of motion. Time series, phase plane portrait, Poincaré map, bifurcation diagrams, and Lyapunov exponents were used to analyze the nonlinear dynamic behavior of the system. The effects of Coriolis and centrifugal forces due to shaft flexibility were also considered in this study. The results obtained from the numerical analytical tools employed agreed well with each other. As demonstrated, the effect of nonlinearities and gyroscopic moment in Scenario 1 was higher than those in the other scenarios. Therefore, the irregular motion occurred at a lower speed ratio (S = 9.30). In addition, when the disk was placed closer to the shaft mid-span, the range of the sub-harmonic motion decreased and the irregular motion occurred at higher speed ratios (S = 9.81). Also, there were five irregular regions in Scenarios 1 and 2. This is while only the quasi-periodic and regular (period-1) motions were observed in Scenarios 3 and 4, respectively. Finally, when the disk was located at the mid-span of the shaft, the sub-harmonic and chaotic motions were not observed. When the disk was mounted at a place different from the mid-span of the shaft, chaotic vibrations were observed. It is, therefore, of utmost importance to identify these types of vibrations since they cause alternating stresses on the main components of rotating machinery and catastrophic failures. The results of the investigation also indicate that the nonlinear terms can be neglected in the equations of motion when the disk is mounted in the mid-span of the shaft.

APPENDIX A

The Lagrangin expression in discrete form is as

$$
\begin{aligned}
L = \frac{1}{2}\int_0^l \Big\{ & \rho A\Big[(\boldsymbol{\Psi}^{\mathrm{T}}\dot{\mathbf{V}})(\boldsymbol{\Psi}^{\mathrm{T}}\dot{\mathbf{V}}) + (\boldsymbol{\Psi}^{\mathrm{T}}\dot{\mathbf{W}})(\boldsymbol{\Psi}^{\mathrm{T}}\dot{\mathbf{W}}) - 2\Omega(\boldsymbol{\Psi}^{\mathrm{T}}\dot{\mathbf{V}})(\boldsymbol{\Psi}^{\mathrm{T}}\mathbf{W}) + 2\Omega(\boldsymbol{\Psi}^{\mathrm{T}}\dot{\mathbf{W}})(\boldsymbol{\Psi}^{\mathrm{T}}\mathbf{V}) \\
& + \Omega^2(\boldsymbol{\Psi}^{\mathrm{T}}\mathbf{V})(\boldsymbol{\Psi}^{\mathrm{T}}\mathbf{V}) + \Omega^2(\boldsymbol{\Psi}^{\mathrm{T}}\mathbf{W})(\boldsymbol{\Psi}^{\mathrm{T}}\mathbf{W})\Big] + \rho\Big[I_y\left(\Omega^2(\boldsymbol{\Psi}'^{\mathrm{T}}\mathbf{V})(\boldsymbol{\Psi}'^{\mathrm{T}}\mathbf{V}) + (\boldsymbol{\Psi}'^{\mathrm{T}}\dot{\mathbf{W}})(\boldsymbol{\Psi}'^{\mathrm{T}}\dot{\mathbf{W}})\right. \\
& \left. - 2\Omega(\boldsymbol{\Psi}'^{\mathrm{T}}\mathbf{V})(\boldsymbol{\Psi}'^{\mathrm{T}}\dot{\mathbf{W}})\right) + I_z\left(\Omega^2(\boldsymbol{\Psi}'^{\mathrm{T}}\mathbf{W})(\boldsymbol{\Psi}'^{\mathrm{T}}\mathbf{W}) + (\boldsymbol{\Psi}'^{\mathrm{T}}\dot{\mathbf{V}})(\boldsymbol{\Psi}'^{\mathrm{T}}\dot{\mathbf{V}}) + 2\Omega(\boldsymbol{\Psi}'^{\mathrm{T}}\mathbf{W})(\boldsymbol{\Psi}'^{\mathrm{T}}\dot{\mathbf{V}})\right) \\
& + J_p\left(\Omega^2 + (\boldsymbol{\Psi}'^{\mathrm{T}}\mathbf{V})(\boldsymbol{\Psi}'^{\mathrm{T}}\mathbf{V})(\boldsymbol{\Psi}'^{\mathrm{T}}\dot{\mathbf{W}})(\boldsymbol{\Psi}'^{\mathrm{T}}\dot{\mathbf{W}}) + 2\Omega(\boldsymbol{\Psi}'^{\mathrm{T}}\mathbf{V})(\boldsymbol{\Psi}'^{\mathrm{T}}\dot{\mathbf{W}})\right)\Big] \\
& - EI\Big[(\boldsymbol{\Psi}''^{\mathrm{T}}\mathbf{V})(\boldsymbol{\Psi}''^{\mathrm{T}}\mathbf{V}) + (\boldsymbol{\Psi}''^{\mathrm{T}}\mathbf{W})(\boldsymbol{\Psi}''^{\mathrm{T}}\mathbf{W})\Big]\Big\}\, dx + \frac{m_d}{2}\Big[(\boldsymbol{\Psi}^{\mathrm{T}}\dot{\mathbf{V}})(\boldsymbol{\Psi}^{\mathrm{T}}\dot{\mathbf{V}}) \\
& + (\boldsymbol{\Psi}^{\mathrm{T}}\dot{\mathbf{W}})(\boldsymbol{\Psi}^{\mathrm{T}}\dot{\mathbf{W}}) - 2\Omega(\boldsymbol{\Psi}^{\mathrm{T}}\mathbf{W})(\boldsymbol{\Psi}^{\mathrm{T}}\dot{\mathbf{V}}) + 2\Omega(\boldsymbol{\Psi}^{\mathrm{T}}\mathbf{V})(\boldsymbol{\Psi}^{\mathrm{T}}\dot{\mathbf{W}}) + \Omega^2(\boldsymbol{\Psi}^{\mathrm{T}}\mathbf{V})(\boldsymbol{\Psi}^{\mathrm{T}}\mathbf{V}) \\
& + \Omega^2(\boldsymbol{\Psi}^{\mathrm{T}}\mathbf{W})(\boldsymbol{\Psi}^{\mathrm{T}}\mathbf{W})\Big]\Big|_{x=l_d} + \frac{\rho_d h}{2}\Big[I_{yd}\left(\Omega^2(\boldsymbol{\Psi}'^{\mathrm{T}}\mathbf{V})(\boldsymbol{\Psi}'^{\mathrm{T}}\mathbf{V}) + (\boldsymbol{\Psi}'^{\mathrm{T}}\dot{\mathbf{W}})(\boldsymbol{\Psi}'^{\mathrm{T}}\dot{\mathbf{W}})\right. \\
& \left. - 2\Omega(\boldsymbol{\Psi}'^{\mathrm{T}}\dot{\mathbf{W}})(\boldsymbol{\Psi}'^{\mathrm{T}}\mathbf{V})\right) + I_{zd}\left(\Omega^2(\boldsymbol{\Psi}'^{\mathrm{T}}\mathbf{W})(\boldsymbol{\Psi}'^{\mathrm{T}}\mathbf{W}) + (\boldsymbol{\Psi}'^{\mathrm{T}}\dot{\mathbf{V}})(\boldsymbol{\Psi}'^{\mathrm{T}}\dot{\mathbf{V}}) + 2\Omega(\boldsymbol{\Psi}'^{\mathrm{T}}\dot{\mathbf{V}})(\boldsymbol{\Psi}'^{\mathrm{T}}\mathbf{W})\right) \\
& + J_{pd}\left(\Omega^2 + (\boldsymbol{\Psi}'^{\mathrm{T}}\mathbf{V})(\boldsymbol{\Psi}'^{\mathrm{T}}\mathbf{V})(\boldsymbol{\Psi}'^{\mathrm{T}}\dot{\mathbf{W}})(\boldsymbol{\Psi}'^{\mathrm{T}}\dot{\mathbf{W}}) + 2\Omega(\boldsymbol{\Psi}'^{\mathrm{T}}\mathbf{V})(\boldsymbol{\Psi}'^{\mathrm{T}}\dot{\mathbf{W}})\right)\Big]\Big|_{x=l_d}
\end{aligned}
\tag{A.1}
$$

The constant matrices in Eqs. (20) ~ (25) defined as

$$\boldsymbol{\Lambda}_1 = \int_0^l \left(\boldsymbol{\Psi}(x)\boldsymbol{\Psi}^T(x)\right) dx \tag{A.2}$$

$$\boldsymbol{\Lambda}_2 = \int_0^l \left(\boldsymbol{\Psi}'(x)\,\boldsymbol{\Psi}'^T(x)\right) dx \tag{A.3}$$

$$\boldsymbol{\Lambda}_3 = \int_0^l \left(\boldsymbol{\Psi}''(x)\,\boldsymbol{\Psi}''^T(x)\right) dx \tag{A.4}$$

$$\boldsymbol{\Lambda}_{d1} = (\boldsymbol{\Psi}_d(x = l_d)(\boldsymbol{\Psi}_d^T(x = l_d)) \tag{A.5}$$

$$\boldsymbol{\Lambda}_{d2} = (\boldsymbol{\Psi}'_d(x = l_d)(\boldsymbol{\Psi}'^T_d(x = l_d)) \tag{A.6}$$

https://doi.org/10.1017/jmech.2012.61 Published online by Cambridge University Press

REFERENCES

1. Jerrelind, J. and Stensson, A., "Nonlinear Dynamics of Parts in Engineering Systems," *Chaos, Solitons and Fractals*, **11**, pp. 2413–2428 (2000).
2. Chang, C. O. and Cheng, J. W., "Nonlinear Dynamics and Instability of a Rotating Shaft-Disk System," *Journal of Sound and Vibration*, **160**, pp. 433–454 (1993).
3. Hosseini, S. A. A. and Khadem, S. E., "Analytical Solution for Primary Resonances of a Rotating Shaft with Stretching Non-Linearity," *IMechE, Journal of Mechanical Engineering Science*, **222**, Part C, pp. 1655–1663 (2008).
4. Hosseini, S. A. A. and Khadem, S. E., "Free Vibrations Analysis of a Rotating Shaft with Nonlinearities in Curvature and Inertia," *Mechanism and Machine Theory*, **44**, pp. 272–288 (2009).
5. Łuczko, J., "A Geometrically Nonlinear Model of Rotating Shafts with Internal Resonance and Self-Excited Vibration," *Journal of Sound and Vibration*, **255**, pp. 433–456 (2002).
6. Qian, D. and Chen, Y. S., "Bifurcation of a Shaft with Hysteretic-Type Internal Friction Force of Material," *Applied Mathematics and Mechanics*, **24**, pp. 638–645 (2003).
7. Pavlović, R., Kozić, P., Mitić, S. and Pavlović, I., "Stochastic Stability of a Rotating Shaft," *Archives of Applied Mechanics,* **79**, pp. 1163–1171 (2009).
8. Dimentberg, M. F. and Naess, A., "Nonlinear Vibrations of a Rotating Shaft with Broadband Random Variations of Internal Damping," *Nonlinear Dynamics*, **51**, pp. 199–205 (2008).
9. Cheng, M., Meng, G. and Jing, J., "Non-Linear Dynamics of a Rotor-Bearing-Seal System," *Archives of Applied Mechanics*, **76**, pp. 215–227 (2006).
10. Nataraj, C. and Harsha, S. P., "The Effect of Bearing Cage Run-Out on the Nonlinear Dynamics of a Rotating Shaft," *Communications in Nonlinear Science and Numerical Simulation*, **13**, pp. 822–838 (2008).
11. Chang-Jian, C. W. and Chen, C. K., "Chaotic Response and Bifurcation Analysis of a Flexible Rotor Supported by Porous and Non-Porous Bearings with Nonlinear Suspension," *Nonlinear Analysis: Real World Applications*, **10**, pp. 1114–1138 (2009).
12. Inayat-Hussain, J. I., "Nonlinear Dynamics of a Statically Misaligned Flexible Rotor in Active Magnetic Bearings," *Communications in Nonlinear Science and Numerical Simulation*, **15**, pp. 764–777 (2010).
13. Muszyńska, A., *Rotor Dynamics*, Taylor & Francis Goup, CRC Press (2005).
14. Khanlo, H. M., Ghayour, M. and Ziaei-Rad, S., "Chaotic Vibration Analysis of Rotating Flexible Continuous Shaft-Disk System with a Rub-Impact Between the Disk and the Stator," *Communications in Nonlinear Science and Numerical Simulation*, **16**, pp. 566–582 (2011).
15. Meirovitch, L., *Principles and Techniques of Vibrations*, Prentice-Hall Inc. (1997).
16. Baruh, H., *Analytical Dynamics*, WCB/McGraw-Hill, pp. 559–563 (1999).
17. Abdul Azeez, M. F. and Vakakis, A. F., "Numerical and Experimental Analysis of a Continuous Overhung Rotor Undergoing Vibro-Impact," *International Journal of Non-linear Mechanics*, **34**, pp. 415–435 (1999).
18. Lee, H. P., "Dynamic Response of a Rotating Timoshenko Shaft Subject to Axial Forces and Moving Loads," *Journal of Sound and Vibration*, **181**, pp. 169–177 (1995).
19. Nayfeh, A. H. and Balachandran, B., *Applied Nonlinear Dynamics*, John Wiley and Sons Inc. (1995).
20. Xu, J. X., "Some Advances on Global Analysis of Nonlinear Systems," *Chaos, Solitons and Fractals*, **39**, pp. 1839–1848 (2009).
21. Wolf, A., Swift, J. B., Swinney, H. L. and Vastano, J. A., "Determining Lyapunov Exponents from a Time Series," *Physica D*, **16**, pp. 285–317 (1985).

(Manuscript received March 1, 2011,
accepted for publication April 12, 2012.)

https://doi.org/10.1017/jmech.2012.61 Published online by Cambridge University Press